

PAPER • OPEN ACCESS

Enlightening the temperature coefficient of triple mesoscopic $\text{CH}_3\text{NH}_3\text{PbI}_{3-x}\text{Cl}_x/\text{NiO}$ and double mesoscopic $\text{CsFAMAPbI}_{3-x}\text{Br}_x/\text{CuSCN}$ carbon perovskite solar cells

To cite this article: Shubhramshu Bhandari *et al* 2023 *J. Phys. Energy* **5** 025006

View the [article online](#) for updates and enhancements.

You may also like

- [Layered perovskite materials: key solutions for highly efficient and stable perovskite solar cells](#)
Chintam Hanmandlu, Anupriya Singh, Karunakara Moorthy Boopathi *et al.*
- [Highly efficient bifacial semitransparent perovskite solar cells based on molecular doping of CuSCN hole transport layer](#)
Shixin Hou, , Biao Shi *et al.*
- [Review—Emerging Applications of g-C₃N₂ Films in Perovskite-Based Solar Cells](#)
Vandana Nagal, Virendra Kumar, Rafiq Ahmad *et al.*



PAPER

OPEN ACCESS

RECEIVED
8 January 2023REVISED
28 February 2023ACCEPTED FOR PUBLICATION
13 March 2023PUBLISHED
23 March 2023

Original content from this work may be used under the terms of the [Creative Commons Attribution 4.0 licence](https://creativecommons.org/licenses/by/4.0/).

Any further distribution of this work must maintain attribution to the author(s) and the title of the work, journal citation and DOI.



Enlightening the temperature coefficient of triple mesoscopic $\text{CH}_3\text{NH}_3\text{PbI}_{3-x}\text{Cl}_x/\text{NiO}$ and double mesoscopic $\text{CsFAMAPbI}_{3-x}\text{Br}_x/\text{CuSCN}$ carbon perovskite solar cells

Shubhranshu Bhandari^{1,*} , Tapas Kumar Mallick¹ and Senthilarasu Sundaram²¹ Environment and Sustainability Institute (ESI), Penryn Campus, University of Exeter, Cornwall TR10 9FE, United Kingdom² Electrical and Electronics Engineering, School of Engineering and the Built Environment, Edinburgh Napier University, Edinburgh EH10 5DT, United Kingdom

* Author to whom any correspondence should be addressed.

E-mail: shubhranshu0094@gmail.com and s.bhandari@exeter.ac.uk**Keywords:** temperature coefficient, double mesoscopic, triple mesoscopic, mixed halide, triple cation

Abstract

Temperature is one of the most crucial outdoor variables that influence the photovoltaic performance and stability of carbon perovskite solar cells (CPSCs), although not many reports are there on temperature-dependent CPSCs performance based on various mesoscopic structures. This study demonstrates the temperature coefficient (T_C) of carbon-based triple and double mesoscopic devices having MAPICL [$\text{MAPbI}_{3-x}\text{Cl}_x$] and CSFAMA [$\text{Cs}_{0.05}(\text{FA}_{0.83}\text{MA}_{0.17})_{0.95}\text{Pb}(\text{I}_{0.83}\text{Br}_{0.17})_3$] to understand the performance compatibility of different CPSC configurations despite the thermal treatment (MA = methylammonium, FA = formamidinium). While treating a single device in the range of 5 °C–65 °C, MAPICL-based CPSC maintained a power conversion efficiency (PCE) of ~9%–11.7%. In contrast, CSFAMA-based double mesoscopic devices showed a PCE variation of ~14%–16% in the same temperature window. The interesting fact of this analysis is that the average T_C values for MAPICL and CSFAMA are in the order of 10^{-4} , implying better retention of performance for both mesoscopic devices despite thermal stress. A photoluminescence analysis has been done to understand the temperature-dependent charge transfer properties between the perovskite and transport layer. To the best of our knowledge, this analysis, for the first time, provides insight into the temperature coefficient of different CPSC mesoscopic structures to promote suitable future development.

1. Introduction

Innovation and advanced technologies of perovskite solar cells (PSCs) have been universally praised as an economically and environmentally feasible renewable solution in the area of orthodox and conventional solar cell technologies to address global challenges in eco-friendly power generation [1–3]. With the progress of materials used as the electron transport layer (ETL), hole transport layer, perovskite layer, and counter electrode, single-junction PSC achieved an outstanding power conversion efficiency (PCE) of >25% [4–20]. These massive developments become pale due to the issues like upscaling, toxicity, and stability, which hold PSCs from practical day-to-day utilization [2, 21]. Various strategies have been applied to resolve the stability issues of halide perovskites, which also leads to the implementation of cost-effective, environmentally superior, and moisture-protective carbon materials as the charge transport layer, and the counter electrode deploying different polymorphs like fullerene, carbon nanotube, graphene, graphite [22–24]. Carbon counter electrode-based PSCs (CPSC) achieved an excellent PCE of >16%, which can attain even higher efficiencies at a lower cost of production [25, 26]. Like every perovskite device, CPSC's outdoor performance and stability dramatically depend on temperature. Usually, physical parameters like surface tension, bandgap, charge diffusion and/or recombination processes are greatly influenced by temperature variation [27]. Most of the temperature-related studies of perovskites are based on noble electrode materials-based devices that

reveal the accumulation of ions in selective interfacial contacts during temperature stress [28–37]. There are hardly any research works related to temperature-dependent performance variation of CPSCs, which is very important to understand the temperature effect on various designs of CPSCs. In this regard, understanding the temperature coefficients (T_C) of various photovoltaic parameters is highly significant considering the effect of specific heat capacities of different materials [38–41]. Interestingly, positive and negative T_C values imply an increase in performance with the increase in temperature and diminished performance with the rise in temperature, respectively [42]. α -Si, CdTe and copper indium gallium selenide are the most widely commercialized thin-film solar cells, which show a negative value of the T_C [43, 44]. In contrast, reports on T_C value evaluation are hardly explored for CPSCs depending on the various possible structures and integrated materials. Due to the possibilities of different mesoscopic designs, evaluation of T_C will not only help in the long-term marketization of CPSCs but also indicate charge transport property at a particular temperature. It will also help in the practical implementation of CPSC at different climatic conditions, as devices in real-world situations work at much higher or lower temperatures related to the standard temperature conditions [45].

Therefore, in this work, two different patterns of CPSC were fabricated to understand their effectiveness at variable temperature conditions with the determination of T_C . As per our previous report, the carbon counter electrode was prepared using graphitic carbon nanoparticles and carbon nanotubes for better performance in ambient conditions which is mentioned in the method section [46, 47]. One set of devices followed the double mesoscopic pattern of FTO/c-TiO₂/m-TiO₂/m-ZrO₂/CSFAMA [Cs_{0.05}(FA_{0.83}MA_{0.17})_{0.95}Pb(I_{0.83}Br_{0.17})₃]/CuSCN/carbon. On the other hand, triple mesoscopic FTO/c-TiO₂/m-TiO₂/m-ZrO₂/m-NiO/MAPbI_{3-x}Cl_x [MAPICL]/carbon was the structure of another set of devices. The effect of temperature on the charge transport and its influence on the performance outcome of CPSCs was analyzed in the temperature range of 5 °C to 65 °C. In every case, a single device was characterized at the above-mentioned temperature window, which enlightened the T_C values of various photovoltaic parameters. Instead of the traditional encapsulation, the carbon-back contact was targeted as a protective layer for the devices. This finding can be relevant for industrial applications in both single-junction and tandem architectures for CPSC devices in future.

2. Method

2.1. Triple mesoscopic device fabrication

The first step was the etching and cleaning of FTO glass samples, which was followed by the deposition of the TiO₂ blocking layer via the spin-coating method at 2000 rpm (rotation per minute) for 30 s (seconds) and heating at 415 °C for 30 min (minutes). The next step was spin-coating the mesoporous TiO₂ (m-TiO₂) (the weight ratio of TiO₂ Dyesol paste and ethanol is 1:6) at 4000 rpm for 30 s, followed by annealing at 500 °C for an hour. After cooling to room temperature, Lithium (trifluoromethane sulfonyl) imide (LITFSI) in acetonitrile (0.1 M) solution was spin-coated (3500 rpm for 30 s) on top of the m-TiO₂ layer followed by heating at 400 °C for half an hour. Next, the ZrO₂ mesoporous layer was spin-coated with diluted ZrO₂ paste at 4000 rpm for 30 s and heated at 400 °C for 30 min. Then, the NiO layer was deposited using nano-oxide-based paste at 4000 rpm for 30 s and sintered at 400 °C for 30 min. The preheated MAPICL precursor solution (~50 μ l) was spin-coated at 2000 rpm for 30 s, followed by heating at 90 °C for 2 h on a preheated hot plate. The low-temperature carbon paste was prepared following our previous study, which contains graphitic carbon nanoparticles instead of commercial carbon black and deposited by blade coating on a selective area on the device and heated at 100 °C for 5 min [47]. Finally, single-walled carbon nanotube was sprayed to achieve better moisture stability due to its hydrophobic nature [48].

2.2. Double mesoscopic device fabrication

The fabrication was adopted from previous literature with suitable modifications [49]. A compact layer of TiO₂ was subsequently deposited via spin-coating at 450 °C from a precursor solution of titanium di-isopropoxide bis(acetylacetonate) (Sigma-Aldrich) diluted in anhydrous ethanol (1:7, volume ratio). A mesoporous TiO₂ layer was then deposited by spin coating a diluted paste at a spin speed of 4000 rpm for 30 s onto the substrate containing TiO₂ compact layer. This was followed by sintering the substrates at 450 °C for 30 min. For Li treatment of the mesoporous TiO₂ scaffold, 150 μ l of LiTFSI (10 mg ml⁻¹, freshly prepared in an inert atmosphere) was spin-coated (3000 rpm). Thereafter, Li-treated substrates were subjected to a second sintering step at 450 °C for 30 min in dry air. Next, the ZrO₂ mesoporous layer was spin-coated with diluted ZrO₂ paste at 4000 rpm for 30 s and heated at 400 °C for 30 min. After cooling down for perovskite deposition, the substrates were transferred to a nitrogen glove box (humidity < 1%). The CSFAMA precursor solution was then spin-coated in a two-step programme at 1000 and 5000 r.p.m. for 10 and 30 s, respectively. During the second step, 100 μ l of chlorobenzene (99.8%, Acros) was dropped on

the spinning substrate 10 s prior to the end of the programme. This was followed by annealing the films at 100 °C for 30 min. Next, CuSCN (35 mg in 1 ml diethyl sulfide) layer was spin-coated at 4000 rpm for 30 s. Finally, the low-temperature carbon paste was deposited by blade coating on a particular area on the device and heated at 100 °C for 5 min.

2.3. Characterization

X-ray diffraction (XRD) was performed on an X'pert pro-MPD XRD of PANalytical with Cu K α 1 radiation ($\lambda = 1.5406 \text{ \AA}$). The cross-sectional layer thickness measurements of the PSC were recorded on a scanning electron microscope (SEM) (LEO 430i, Carl Zeiss). The charge-transport properties of different ETLs on perovskite were measured by photoluminescence spectroscopy (PL: FLS1000 Photoluminescence Spectrometer, Edinburgh instruments). All photovoltaic measurements of the CPSC were executed under 1000 W m⁻² of light illumination from a Wacom AAA continuous solar simulator (model type: WXS-210S-20, AM1.5G) and an EKO MP-160i I–V Tracer. Electrochemical impedance spectroscopy (EIS) assessment was performed with an AUTOLAB frequency analyzer setup equipped with an AUTOLAB PGSTAT-10, and a frequency response analyzer module under one sun condition having a frequency range from 1 MHz to 10 mHz at the 0.80 V open-circuit voltage. The EC-lab software was used to fit the experimental data. Incident photon to electron conversion efficiency (IPCE) measurement was carried out on a BENTHAM PVE300 Photovoltaic external quantum efficiency (EQE) and internal quantum efficiency (IQE) solution under 300–850 nm wavelength using a tungsten halogen lamp source. The photovoltaic measurement was carried out in a reverse-biased condition for all fabricated devices, and temperature-related performance was carried out under an ambient environment. For the temperature-related performance check, each device was examined in the temperature window of 5 °C–65 °C and kept at a particular temperature for 30 min before further characterization.

3. Results and discussion

3.1. Optical, microstructural characterization

Initially, optical and microstructural characterizations of materials were performed for different device types. The XRD of the MAPbI_{3-x}Cl_x (MAPICL) was analyzed to confirm the mixed halide perovskite formation. The characteristic peaks at ~14°, 28°, 32°, 41° and 44° confirms the formation MAPbI_{3-x}Cl_x, as shown in figure 1(a) [50]. Similarly, the XRD of the CSFAMA was analyzed to confirm the formation of triple-cation perovskite, and the observed peaks at ~14°, 20°, 25°, 29°, 32°, 35°, 41° and 43° verify the formation of CSFAMA, as shown in figure 1(b) [51]. Next, the cross-sectional SEM of the champion MAPICL device was tested to verify the perfect coating of different layers and the thickness of the layers. Figure 1(c) shows the distinctive nature of the TiO₂ (~200 nm), ZrO₂ (~250 nm), NiO (~300 nm), and MAPICL (~300 nm) layers in the device. Again, the CSFAMA-based champion device was investigated using the cross-sectional SEM to confirm the discrete layer structure of the cell. Figure 1(d) demonstrates the distinctive pattern of the TiO₂ (~200 nm), ZrO₂ (~250 nm), perovskite (~350 nm), thin CuSCN (~70 nm) and carbon layers in the device.

3.2. Photovoltaic performances under different thermal conditions for MAPICL devices

Significant photovoltaic performance was observed for the MAPICL devices under various thermal stress. The achieved PCE for the champion CPSC device at 25 °C was 11.7%, and a small decrease was observed when the temperature was raised or lowered from room temperature (25 °C). Figure 2(a) and table 1 describe the major *J*–*V* characteristics at different temperatures for the champion device, respectively. Because a single device was characterized at different temperatures, it was essential to see the effect of the temperature cycle from high to low to high temperature. In this respect, the result shown in figure 2(b) implies the good reversible performance of the devices even after two complete cycles, indicating the high stability of MAPICL despite temperature stress. Consequently, the loss of PCE for MAPICL devices in the temperature range of 5 °C–65 °C is shallow, which implies stability at relatively high and low temperatures. The temperature behavior vastly relies on the stability issues of the films and charge transport property. The oxide layers stay ineffective with temperature in the examined temperature range, although halide perovskites are always vulnerable to temperature stress, and reports indicate possible degradation at much lower temperatures than expected [33]. The chloride-based mixed halide perovskite has been traditionally observed as more air-stable, and PCEs observed also suggested only ~1% change from room temperature to 55 °C [52].

Finding the consistency of device performance is extremely important for any particular type of solar cell. In this respect, the performance of 5 MAPICL devices was measured, and the result is given in figure 3 in the form of box-whiskers plots. Not much deviation of *J*_{SC}, *V*_{OC}, FF and PCE was found for different devices.

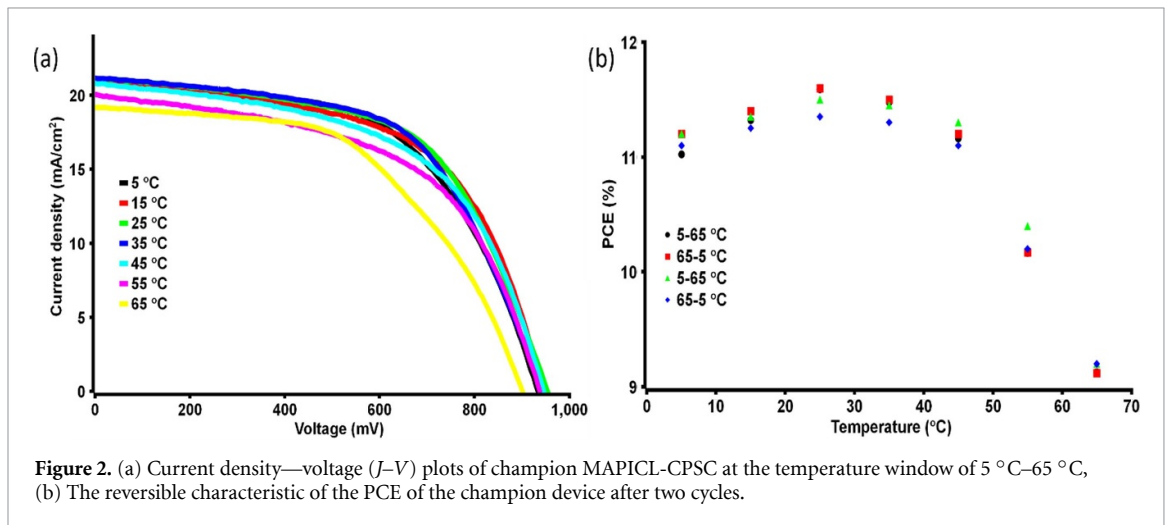
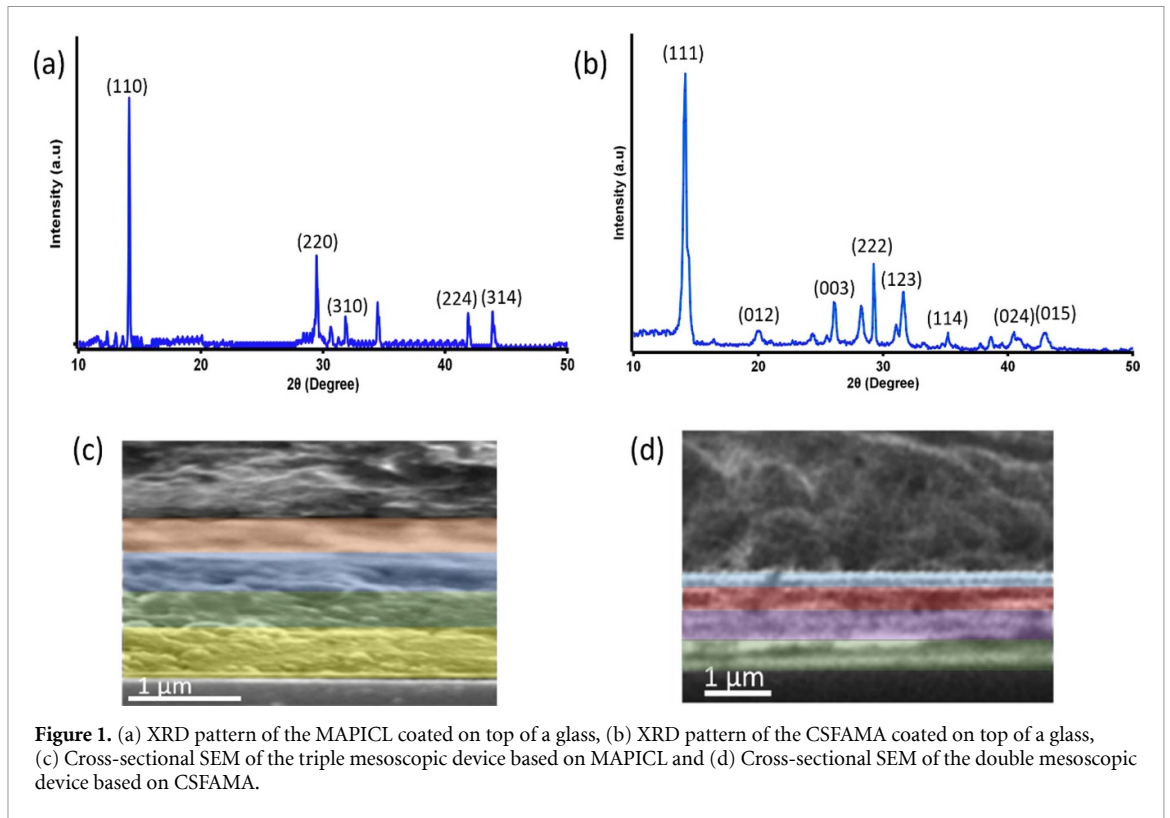
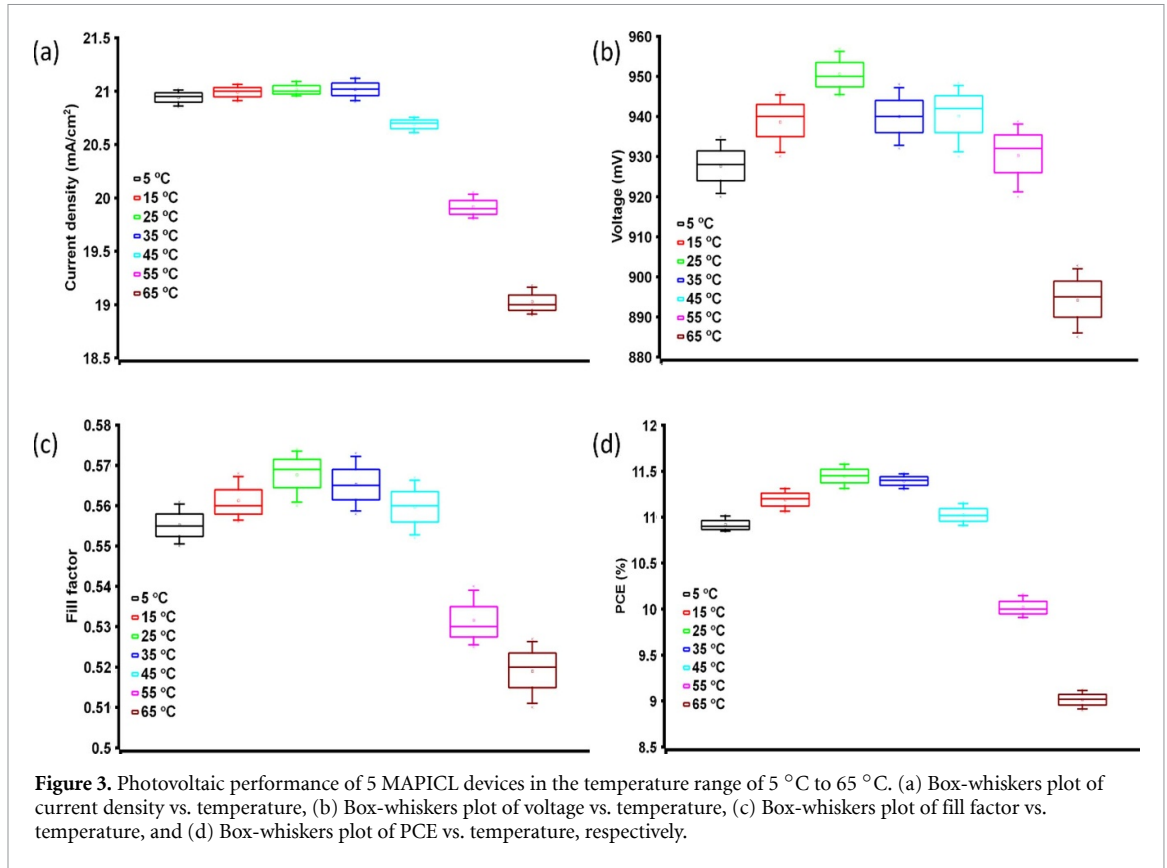


Table 1. Photovoltaic parameters of MAPICL-CPSC under 1 SUN 1.5G AM (active area of 0.12 cm²).

Temperature (°C)	J_{SC} (mA cm ⁻²)	V_{OC} (mV)	FF	PCE (%)
5	21.05	935.5	0.56	11.0
15	21.07	947	0.565	11.3
25	21.3	958.2	0.576	11.7
35	21.2	945	0.572	11.4
45	20.7	950.1	0.566	11.13
55	20.06	939.1	0.55	10.3
65	19.2	903.1	0.526	9.12

3.3. Evaluation and analysis of temperature coefficients for MAPICL devices

As device structure and materials influence the pattern of temperature-related photovoltaic performance, determining the temperature coefficient (T_C) of CPSC devices applying the generalized linear relation is essential for a better understanding of temperature and J – V correlation in real-world conditions, as mentioned in the following equations (1)–(3) [39, 53]



$$J_{TC} = (\Delta J / \Delta T) 1 / J_{ref} \quad (1)$$

$$V_{TC} = (\Delta V / \Delta T) 1 / V_{ref} \quad (2)$$

$$\eta_{TC} = (\Delta \eta / \Delta T) 1 / \eta_{ref} \quad (3)$$

where, J_{TC} represents the T_C of current density, ΔJ represents the difference between the short-circuit current density at the concerned temperature and reference temperature (reference temperature is 25 °C), J_{ref} means current density at the reference temperature, V_{TC} means the T_C of open-circuit voltage, ΔV represents the difference between the open-circuit voltage at a concerned temperature and the reference temperature, V_{ref} means the open-circuit voltage at the reference temperature, η_{TC} represents the T_C of efficiency, $\Delta \eta$ represents the efficiency difference at a particular temperature concerning the reference temperature, η_{ref} depicts the efficiency at the reference temperature, and ΔT defines the temperature difference between the temperature of concern and the reference temperature.

Figure 4 and table 2 show the pattern of T_C values for J_{SC} , V_{OC} , FF and PCE for the champion MAPICL triple mesoscopic device. Observation suggests an increase in the J_{SC} for the champion device from 5 °C to 35 °C and then a decrease from 35 °C to 65 °C, although mostly J_{SC} at 25 °C and 35 °C have really close values. On the other hand, the V_{OC} , FF, and PCE increased from 5 °C to 25 °C and then decreased from 25 °C to 65 °C for all the devices. The average T_C values observed for MAPICL devices are in the order of 10^{-4} , which suggests a shallow change in the parameters with the change in temperature. Usually, the temperature gradient created due to different layers influences the performance of halide-based perovskites driven by ion migration [54]. This ion migration is the primary reason behind the chemical instability of halide perovskites and affects their decomposition at temperatures much lower than degradation conditions, but the presence of mixed halide often makes the perovskite more stable due to reduced ion migration [55]. Although the MAPICL-based devices maintained a nice overall PCE in the process of temperature variation, slight changes were observed as expected due to the cumulative effect of ion migration and accumulation at the interfaces and disruption of the charge transport property [56]. Overall the T_C of MAPICL-based CPSC is fascinating and can be a real competitor for stable perovskite devices in outdoor conditions.

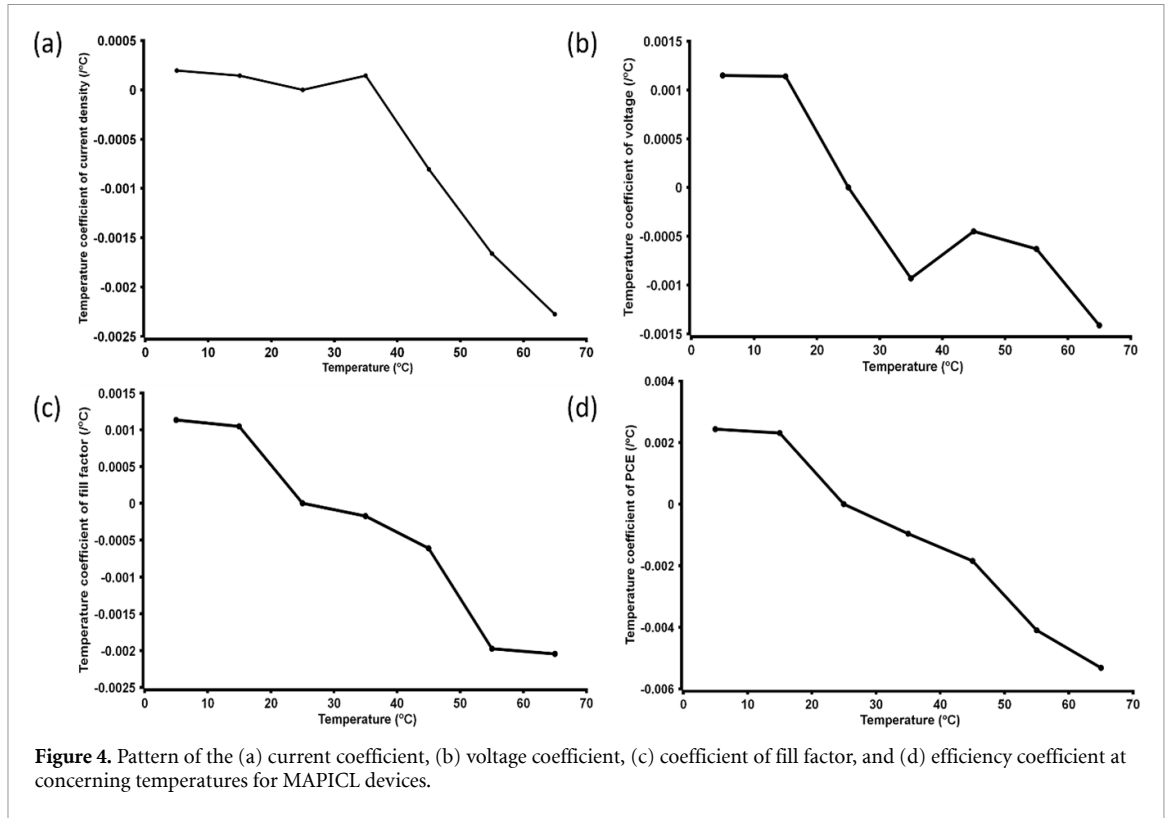


Figure 4. Pattern of the (a) current coefficient, (b) voltage coefficient, (c) coefficient of fill factor, and (d) efficiency coefficient at concerning temperatures for MAPICL devices.

Table 2. Average values of temperature coefficients for MAPICL device.

Temperature (<i>T</i>) range (°C)	Average temperature coefficient of J_{SC}	Average temperature coefficient of V_{OC}	Average temperature coefficient of FF	Average temperature coefficient of PCE_{max}
$5 \leq T \leq 25$	0.000112	0.000763	0.000726	0.001584
$25 \leq T \leq 35$	7.109×10^{-05}	NA	NA	NA
$35 \leq T \leq 65$	-0.001149	NA	NA	NA
$25 \leq T \leq 65$	NA	-0.00068	-0.00096	-0.00244

3.4. Photovoltaic performances under different thermal conditions for CSFAMA devices

The photovoltaic performance was fascinating for the CSFAMA devices. The achieved PCE for the champion CPSC device at 25 °C is ~16%, and it decreases when moved towards the higher or lower temperature regions. Figure 5(a) and table 3 describe the observed J - V characteristics at different temperatures for the champion device, respectively. The performance according to the reversible temperature cycle (from high to low to high temperature) was also observed for the devices. In this matter, the result displayed in figure 5(b) implies the good reversible performance of the device, indicating the high regeneracy of CSFAMA despite temperature stress. On the other side, the loss of PCE for CSFAMA devices in the temperature range of 5 °C–65 °C is quite similar to MAPICL, which implies stability at relatively high and low temperatures despite thermal stress. Finding the repeatability of device performance is vital for any particular type of solar cell. Considering that, the performance of 5 CSFAMA devices was measured, and the result is given in figure 6 in the form of box-whiskers plots. The J_{SC} , V_{OC} , FF, and PCE had slight variations for all the cases, which implies sophisticated and reproducible techniques.

3.5. Evaluation and analysis of temperature coefficients for CSFAMA devices

The temperature coefficient (T_C) was calculated using the standard equations mentioned in an earlier section as (1)–(3). Figure 7 and table 4 show the pattern of T_C values for J_{SC} , V_{OC} , FF and PCE for the CSFAMA-based champion device, which suggests an increase in the J_{SC} from 5 °C to 35 °C, similar to the other MAPICL halide perovskite devices, and then a decrease from 35 °C to 65 °C, although the overall photovoltaic performance is much more pronounced for CSFAMA. Observation related to the V_{OC} , FF, and PCE displayed an increase from 5 °C to 25 °C and then a slight decrease from 25 °C to 65 °C. The average T_C (PCE) values observed for CSFAMA devices are also in the order of 10^{-4} , suggesting a minor change in the parameters with the change in temperature but slightly higher compared to the MAPICL. The analysis also implies the role of carbon counter electrode as a favorable protective layer due to its lesser hydrophilic nature

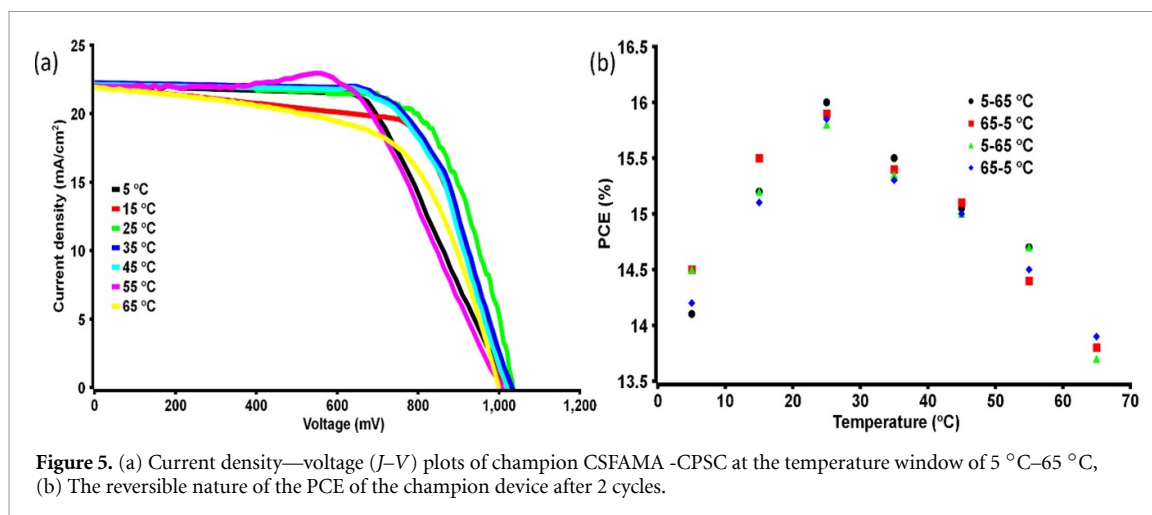


Figure 5. (a) Current density—voltage (J – V) plots of champion CSFAMA-CPSC at the temperature window of 5 °C–65 °C, (b) The reversible nature of the PCE of the champion device after 2 cycles.

Table 3. Photovoltaic parameters of CSFAMA-CPSC under 1 SUN 1.5 G AM (active area of 0.12 cm²).

Temperature (°C)	J_{SC} (mA cm ⁻²)	V_{OC} (mV)	FF	PCE _{max} (%)
5	22.05	1024.9	0.625	14.12
15	22.08	1026.6	0.674	15.27
25	22.2	1035.0	0.694	15.9
35	22.25	1033.2	0.672	15.45
45	22.15	1022.3	0.663	15.0
55	21.9	1015.9	0.659	14.66
65	21.7	1002.6	0.632	13.75

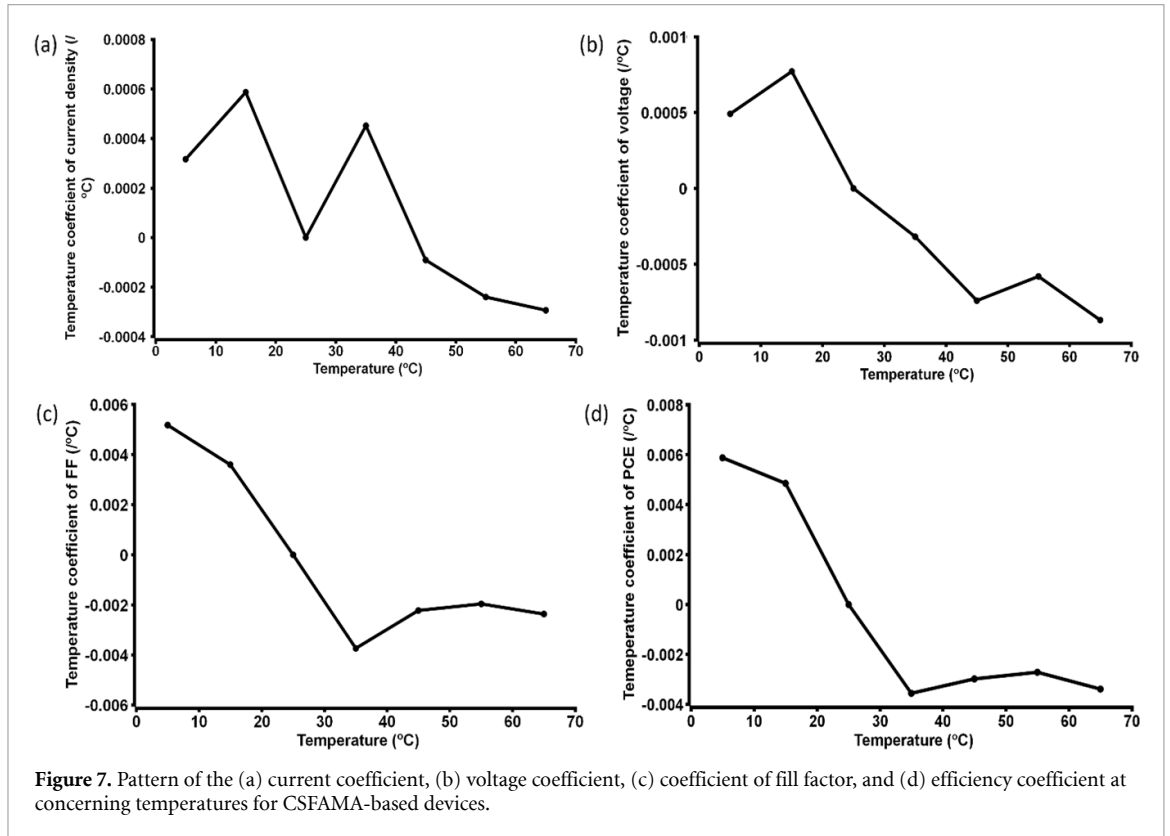
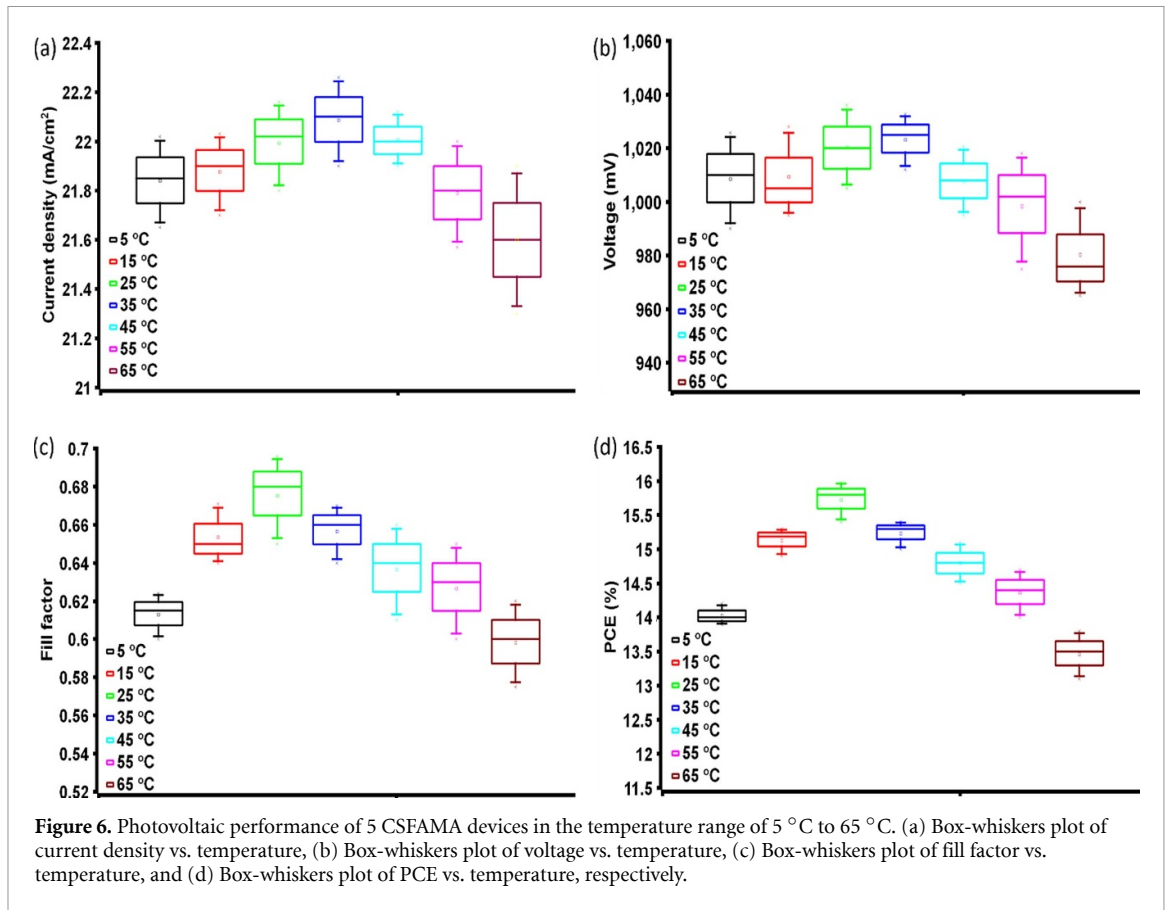
[47]. As the presence of a temperature gradient between the layers significantly influences the performance by altering the charge transport property, an understanding of this phenomenon was carried out utilizing the photoluminescence (PL) study.

3.6. Analysis of MAPICL and CSFAMA device performance by various characterization methods

The photovoltaic performance of MAPICL and CSFAMA devices was scrutinized by incident photon to electron conversion efficiency (IPCE), EIS, steady state PL and time-resolved photoluminescence (TRPL) to understand the critical factors behind the altered performance.

IPCE analysis is not only a valuable tool to demonstrate the quantum efficiency and integrated photocurrent density of the devices, but it can also illustrate the quality of thin films in the devices. IPCE produced integrated photocurrent densities with slightly reduced values compared to J – V characterization due to the effect of optical losses caused by reflection and transmission. According to previous studies, thermal stress can alter the cohesion of the perovskite interfacial contact, influencing the surface defect traps and refining the thin-film quality of perovskite [57]. In figure 8, the IPCE of the two different types of devices is shown at four different temperatures, namely, 5 °C, 25 °C, 45 °C and 65 °C, which illustrates the thin film and interface quality. Usually, better IPCE coverage in the region of ~400 nm–780 nm indicates improved perovskite film and interface quality in contact with the transport layer proving the reduction of surface defects, and figure 8 clarifies the temperature effect on the interface quality.

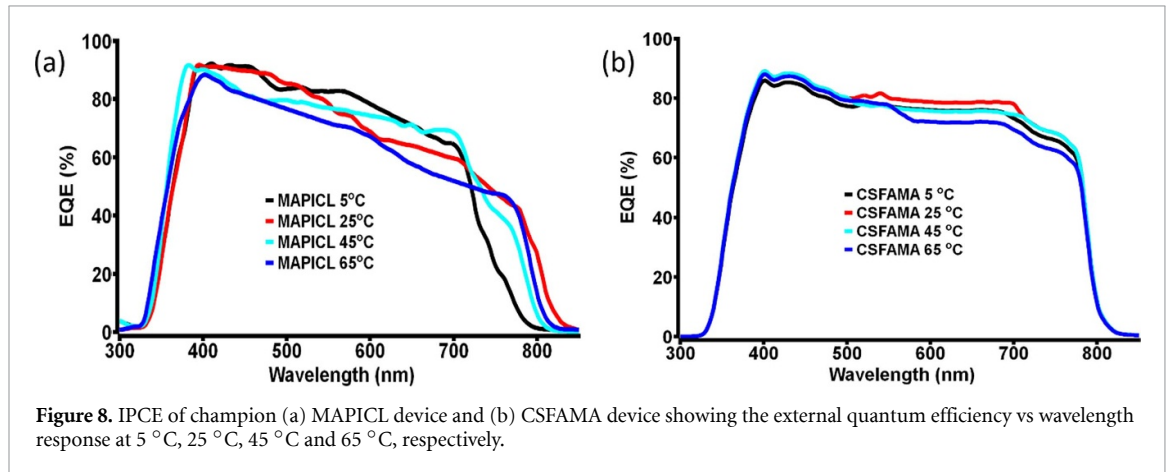
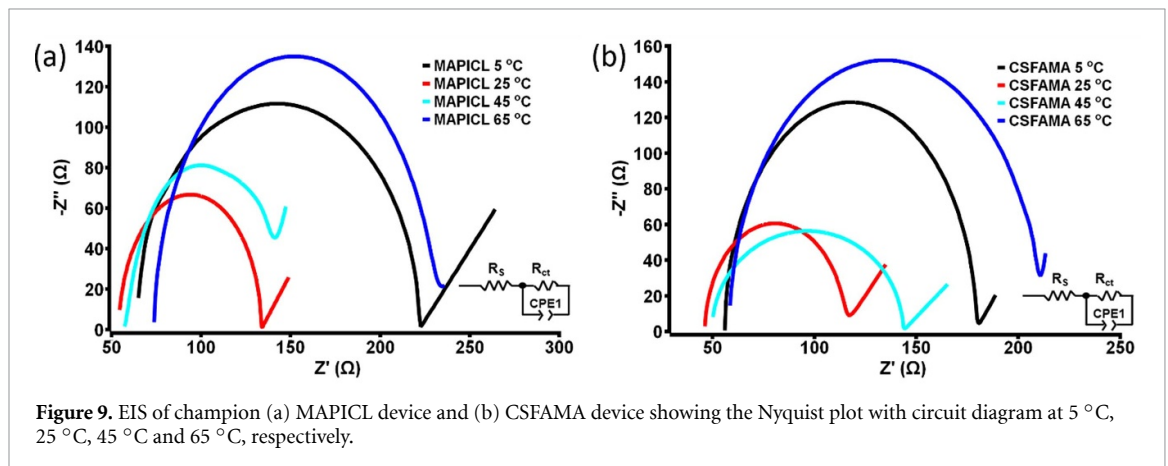
Next, an attempt was made to demonstrate the charge transfer and recombination behavior of the devices using EIS under one sun condition with the help of the Nyquist plot (figure 9). The plot represents the series resistance (R_s) and charge transfer resistance (R_{ct}) of the champion devices at four different temperatures where major changes have been observed. The series resistance (R_s) demonstrates the resistance of both FTO and carbon counter electrode, which is expected to be smaller for a high-performance device. The temperature variation significantly affects the R_s values producing the best performance for the devices at 25 °C. From the EIS plot, the interfacial charge transfer resistance (R_{ct}) between the perovskite and carbon electrode was found to be altered by temperature influence. In the lower temperature (5 °C) and higher temperature (65 °C), both types of device achieved high R_{ct} values (the difference between two intersection points of the parabolic curves along the x -axis). The interfacial resistance increases while increasing and decreasing the temperature from 25 °C, which explains the photovoltaic characteristics as well. This also implies the possibility of charge accumulation at the interface resulting in reduced photovoltaic performance [58].



Further, temperature-dependent PL solidifies the reason behind the variation of photovoltaic parameters with temperature alteration, as shown in figure 10. After excitation of electrons in halide perovskite, they will fall back to the ground state releasing energy in three different ways, namely radiative transition

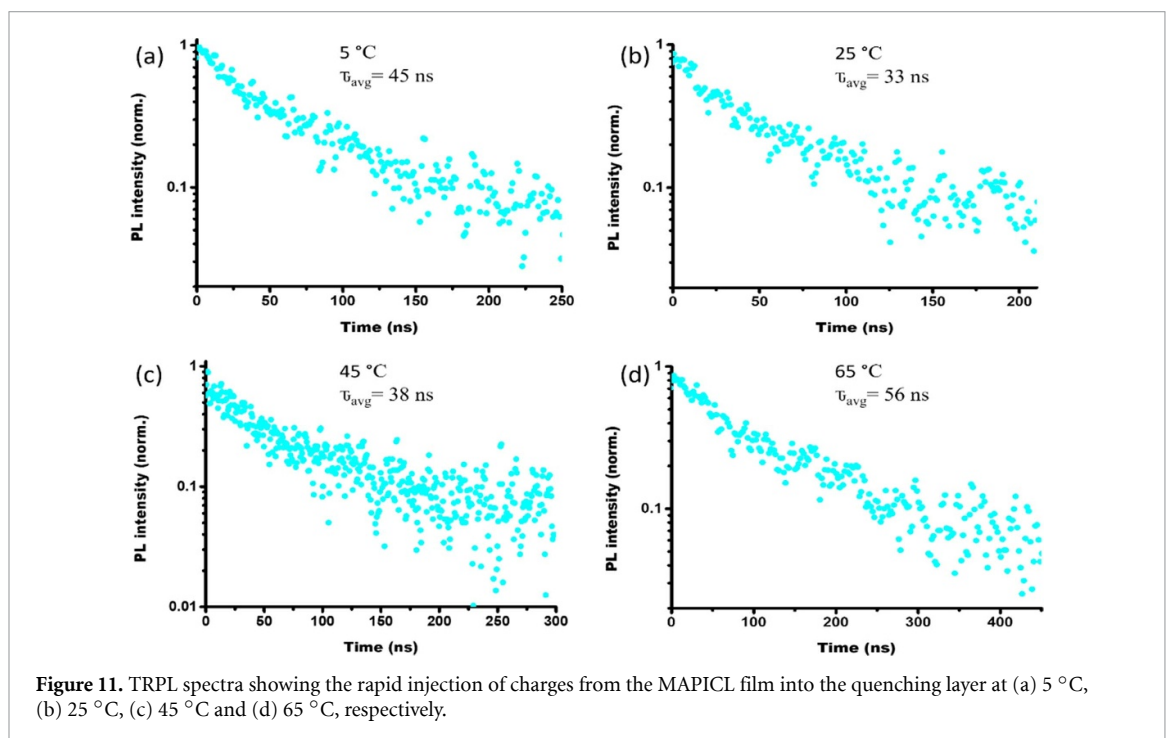
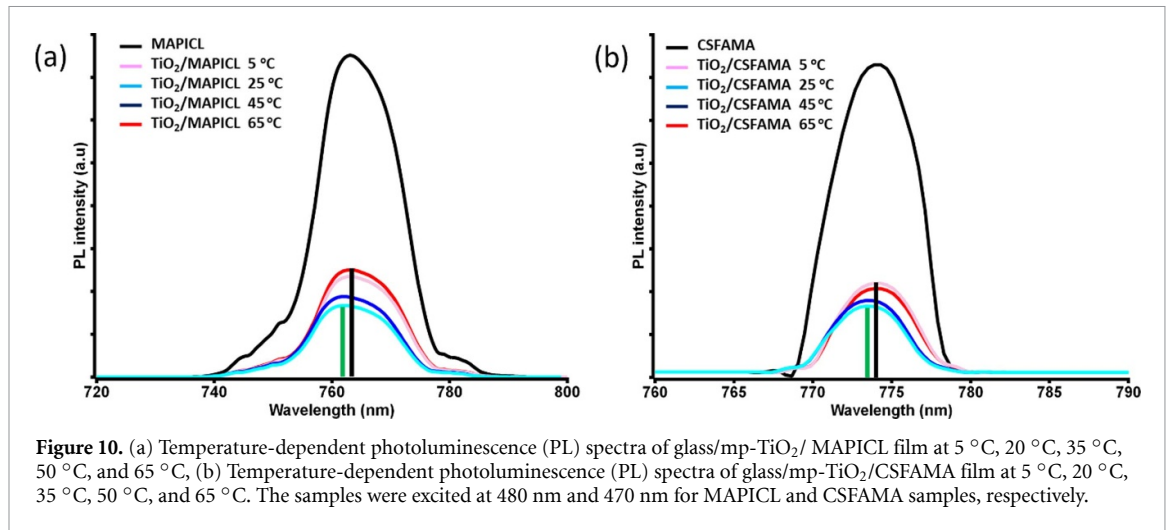
Table 4. Average values of temperature coefficients for the CSFAMA device.

Temperature (T) range (°C)	Average temperature coefficient of J_{SC}	Average temperature coefficient of V_{OC}	Average temperature coefficient of FF	Average temperature coefficient of PCE_{max}
$5 \leq T \leq 25$	0.0003	0.0004	0.0029	0.0035
$25 \leq T \leq 35$	0.0002	NA	NA	NA
$35 \leq T \leq 65$	-0.00004	NA	NA	NA
$25 \leq T \leq 65$	NA	-0.0005	-0.002	-0.0025

**Figure 8.** IPCE of champion (a) MAPICL device and (b) CSFAMA device showing the external quantum efficiency vs wavelength response at 5 °C, 25 °C, 45 °C and 65 °C, respectively.**Figure 9.** EIS of champion (a) MAPICL device and (b) CSFAMA device showing the Nyquist plot with circuit diagram at 5 °C, 25 °C, 45 °C and 65 °C, respectively.

(it resembles PL), non-radiative transition (mostly inter-system crossing or internal conversion) and energy transfer and quenching [49]. In the quenching effect, the excited state electrons of the coated perovskite material will fall back to the ground state by energy transfer to the mesoporous ETLs, which act as the quenching layer. In the absence of a quenching layer, the energy is released by PL mainly, producing the sharpest emission peak of the glass/perovskite film. However, the ETL layer will force the energy of excited electrons to be released by energy transfer and quenching which is critical to understand the quenching layers' charge transfer efficiency [59]. Here, the temperature-dependent PL was examined for TiO₂ and perovskites (MAPICL and CSFAMA) at four different temperatures, namely 5 °C, 25 °C, 45 °C and 65 °C. Both the MAPICL and CSFAMA showed the highest quenching effect at 25 °C, although, at 45 °C, the quenching is quite close, showcasing very low disruption of the charge transfer process, which actually confirms the reason behind stable performance despite thermal stress. The lowest quenching was observed at 5 and 65 °C with a slight red shift of the PL peak.

The red shift of wavelength usually implies vulnerability due to deep-level traps at grain boundaries increasing the recombination centers and affecting the charge transfer efficiency [60]. At the same time, it also indicates a possible change in the band positions, which is actually triggering the recombination process and affecting the charge transfer efficiency [60]. Due to the ion migration and accumulation at the interfaces when a temperature gradient is applied, the charge recombination process becomes more effective, which actually diminishes the photovoltaic outcome, and it was evident from EIS analysis as well [61].



TRPL (time-resolved photoluminescence) was used to consolidate the observations as it estimated the charge carrier dynamics quantitatively. The long average lifetime (τ_{avg}) of the MAPICL and CSFAMA was observed, which was ~ 700 ns and 850 ns, respectively, indicating the high electronic quality of the pristine perovskites. In agreement with the temperature-dependent steady-state PL, the charge carrier lifetime decreased extensively for the perovskite films in the presence of a quenching layer. Figures 11 and 12 explain the faster electron injection from the conduction band of perovskite into the quenching layer at 25 °C. The TRPL also explains stronger electronic interaction between the CSFAMA and TiO₂ compared to MAPICL, resulting in an overall better performance of the caesium-based devices. But for both types of devices, the average lifetime does not alter sharply with the temperature variation, implying very small temperature coefficient values for triple and double mesoscopic devices.

Despite the PL analysis, there can be an effect of the thermal expansion coefficient, which is expected to play a crucial role in diminishing the performance after a certain level of thermal stress by creating pinholes in the perovskite layer sandwiched with the transport layers [62]. Further studies are required on the effect of physical properties like thermal expansion coefficient and specific heat capacities at the interfaces. Overall, it is evident that temperature can considerably impact the photovoltaic parameters of CPSC. The experimental outcome is further suggestive of the CPSCs' photovoltaic character for real-world conditions. A comparison has been provided in table 5, showing the T_C (PCE) variation for different CPSC devices, which suggests the

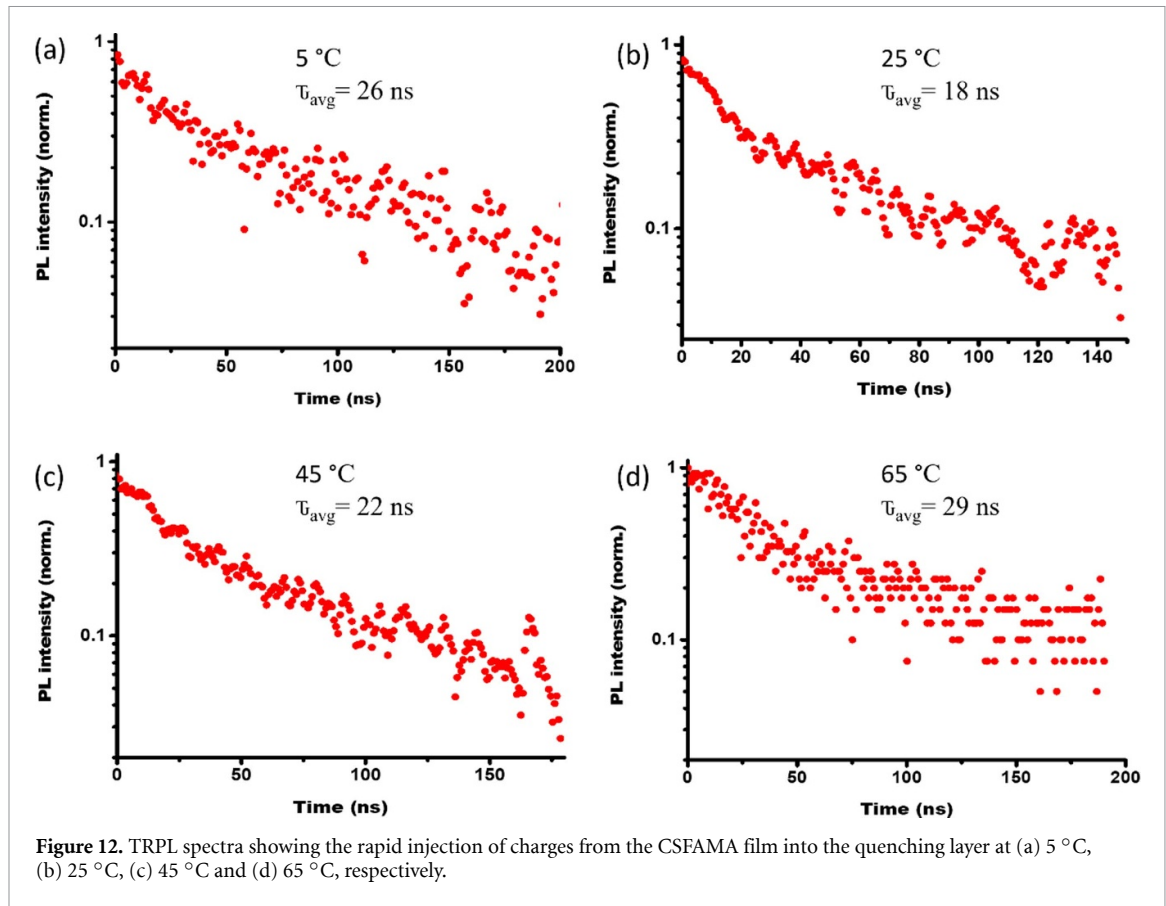


Table 5. Comparison of temperature coefficient for carbon electrode-based unencapsulated perovskite solar cells.

Device	Measuring condition	T_C (PCE)	Reference
PCBM-coated brookite	Ambient	$\approx -0.11\%/^{\circ}\text{C}$	[63]
TiO ₂ /FAPbI ₃ /commercial carbon (planar structure)	Ambient	$\approx -0.17\%/^{\circ}\text{C}$ (25 °C–125 °C)	[63]
Brookite	Ambient	$\approx -0.17\%/^{\circ}\text{C}$ (25 °C–125 °C)	[63]
TiO ₂ /FAPbI ₃ /commercial carbon (planar structure)	Ambient	$\approx -0.35\%/^{\circ}\text{C}$ (25 °C–85 °C)	[59]
TiO ₂ /MAPbI ₃ /NiO/commercial carbon (mesoporous structure)	Ambient	$\approx -1\%/^{\circ}\text{C}$ (25 °C–75 °C)	[56]
TiO ₂ /MAPbI ₃ /WO ₃ -commercial carbon (mesoporous structure)	Ambient	$\approx -0.24\%/^{\circ}\text{C}$ (25 °C–65 °C)	This Work
TiO ₂ /MAPICL/NiO/graphitic carbon/SWCNT (triple mesoporous structure)	Ambient	$\approx -0.25\%/^{\circ}\text{C}$ (25 °C–65 °C)	This work
TiO ₂ /CSFAMA/CuSCN/graphitic carbon/SWCNT (double mesoporous structure)	Ambient	$\approx -0.25\%/^{\circ}\text{C}$ (25 °C–65 °C)	This work

devices of this report are one of the best-reported mesoporous CPSC to date. However, the challenge remains as the fabrication of CPSCs and modules with thermal stress resistance, developed via unorthodox processes and/or architectures, which can address the photovoltaic limitations and ameliorate the cost-effectiveness.

4. Conclusion

CPSC devices can have different configurations depending on various materials utilized, and each particular type shows a distinctive performance behavior. This report investigates CPSC's temperature coefficient for n-i-p structured cells using double and triple mesoscopic architectures with different halide perovskites and hole transport materials MAPICL/NiO and CSFAMA/CuSCN to recognize the temperature behavior of diverse device types. The interesting fact of this analysis is that the average T_C values for MAPICL and

CSFAMA are $\approx -0.24\%/^{\circ}\text{C}$ and $-0.25\%/^{\circ}\text{C}$ in the 25°C – 65°C temperature range, implying high restoration properties in an ambient environment without any encapsulation. The PL analysis demonstrates the diminished charge transfer process due to temperature stress as the reason for reduced device performances. Noticeably, carbon as a protective layer turned out to be an impactful option instead of separate encapsulation, even in harsh experimental conditions. Overall, the impact of T_C on the structure and materials of CPSC will encourage more large-scale development for outdoor testing conditions. We firmly believe the T_C values of other CPSC devices having similar configurations will closely replicate the trend of this study. Future innovation in this field will be influenced by the portrayal of this study to develop more suitable halide perovskites, transport materials and their integration into the device.

Data availability statement

The data cannot be made publicly available upon publication because they are not available in a format that is sufficiently accessible or reusable by other researchers. The data that support the findings of this study are available upon reasonable request from the authors.

Acknowledgments

The partial funding from Engineering and Physical Sciences Research Council (EPSRC) is acknowledged.

Author contributions

Shubhranshu Bhandari: Conceptualization, Methodology, Formal analysis, Investigation, Writing—original draft, Visualization. Tapas Mallick: Writing—review & editing, Supervision, Project administration, Funding acquisition. Senthilarasu Sundaram: Writing—review & editing, Supervision, Project administration, Funding acquisition.

Conflict of interest

There are no conflicts to declare.

ORCID iD

Shubhranshu Bhandari  <https://orcid.org/0000-0002-3347-9682>

References

- [1] Yan J and Saunders B R 2014 Third-generation solar cells: a review and comparison of polymer:fullerene, hybrid polymer and perovskite solar cells *RSC Adv.* **4** 43286–314
- [2] Torabi N, Behjat A, Zhou Y, Docampo P, Stoddard R J, Hillhouse H W and Ameri T 2019 Progress and challenges in perovskite photovoltaics from single- to multi-junction cells *Mater. Today Energy* **12** 70–94
- [3] Sheikh M S, Roy A, Bhandari S, Mallick T K, Sundaram S and Sinha T P 2020 Highly conductive double perovskite oxides A_2LuTaO_6 ($\text{A} = \text{Ba}, \text{Sr}, \text{Ca}$) as promising photoanode material for dye sensitized solar cells *Mater. Lett.* **276** 128220
- [4] Kojima A, Teshima K, Shirai Y and Miyasaka T 2009 Organometal halide perovskites as visible-light sensitizers for photovoltaic cells *J. Am. Chem. Soc.* **131** 6050–1
- [5] Kim H-S et al 2012 Lead iodide perovskite sensitized all-solid-state submicron thin film mesoscopic solar cell with efficiency exceeding 9% *Sci. Rep.* **2** 591
- [6] Grancini G et al 2017 One-Year stable perovskite solar cells by 2D/3D interface engineering *Nat. Commun.* **8** 15684
- [7] Meng F, Liu A, Gao L, Cao J, Yan Y, Wang N, Fan M, Wei G and Ma T 2019 Current progress in interfacial engineering of carbon-based perovskite solar cells *J. Mater. Chem. A* **7** 8690–9
- [8] The National Renewable Energy Laboratory 2022 Best research-cell efficiency chart n.d. (available at: www.nrel.gov/pv/cell-efficiency.html)
- [9] Choi I Y, Kim C U, Park W, Lee H, Song M H, Hong K K, Seok S I and Choi K J 2019 Two-terminal mechanical perovskite/silicon tandem solar cells with transparent conductive adhesives *Nano Energy* **65** 104044
- [10] Siegler T D, Shimpi T M, Sampath W S and Korgel B A 2019 Development of wide bandgap perovskites for next-generation low-cost CdTe tandem solar cells *Chem. Eng. Sci.* **199** 388–97
- [11] Forgacs D, Wojciechowski K and Malinkiewicz O 2020 Perovskite photovoltaics: from laboratory to industry BT *High-Efficient Low-Cost Photovoltaics: Recent Developments* ed V Petrova-Koch, R Hezel and A Goetzberger pp 219–55 (Cham: Springer International Publishing)
- [12] Ghosh A, Bhandari S, Sundaram S and Mallick T K 2020 Carbon counter electrode mesoscopic ambient processed & characterised perovskite for adaptive BIPV fenestration *Renew. Energy* **145** 2151–8
- [13] Lee M M, Teuscher J, Miyasaka T, Murakami T N and Snaith H J 2012 Efficient hybrid solar cells based on meso-superstructured organometal halide perovskites *Science* **338** 643–7
- [14] Abate A, Correa-Baena J-P, Saliba M, Su'ait M S and Bella F 2018 Perovskite solar cells: from the laboratory to the assembly line *Chem. Eur. J.* **24** 3083–100

- [15] Bashir A et al 2018 Spinel Co_3O_4 nanomaterials for efficient and stable large area carbon-based printed perovskite solar cells *Nanoscale* **10** 2341–50
- [16] Batmunkh M, Shearer C J, Biggs M J and Shapter J G 2015 Nanocarbons for mesoscopic perovskite solar cells *J. Mater. Chem. A* **3** 9020–31
- [17] Chen H and Yang S 2017 Carbon-based perovskite solar cells without hole transport materials: the front runner to the market? *Adv. Mater.* **29** 1603994
- [18] Collavini S and Delgado J L 2017 Carbon nanoforms in perovskite-based solar cells *Adv. Energy Mater.* **7** 1601000
- [19] Duan M, Hu Y, Mei A, Rong Y and Han H 2018 Printable carbon-based hole-conductor-free mesoscopic perovskite solar cells: from lab to market *Mater. Today Energy* **7** 221–31
- [20] Meng F, Gao L, Yan Y, Cao J, Wang N, Wang T and Ma T 2019 Ultra-low-cost coal-based carbon electrodes with seamless interfacial contact for effective sandwich-structured perovskite solar cells *Carbon* **145** 290–6
- [21] Wang R, Mujahid M, Duan Y, Wang Z-K, Xue J and Yang Y 2019 A review of perovskites solar cell stability *Adv. Funct. Mater.* **29** 1808843
- [22] Wang X, Liu H, Zhou F, Dahan J, Wang X, Li Z and Shen W 2018 Temperature gradient-induced instability of perovskite via ion transport *ACS Appl. Mater. Interfaces* **10** 835–44
- [23] Roy A, Ghosh A, Bhandari S, Sundaram S and Mallick T K 2020 Realization of poly(methyl methacrylate)-encapsulated solution-processed carbon-based solar cells: an emerging candidate for buildings comfort *Ind. Eng. Chem.* **59** 11063–71
- [24] Bhandari S, Roy A, Mallick T K and Sundaram S 2020 Impact of different light induced effect on organic hole-transporting layer in perovskite solar cells *Mater. Lett.* **268** 127568
- [25] Hadadian M, Småt J-H and Correa-Baena J-P 2020 The role of carbon-based materials in enhancing the stability of perovskite solar cells *Energy Environ. Sci.* **13** 1377–407
- [26] Wang Q, Zhang W, Zhang Z, Liu S, Wu J, Guan Y, Mei A, Rong Y, Hu Y and Han H 2020 Crystallization control of ternary-cation perovskite absorber in triple-mesoscopic layer for efficient solar cells *Adv. Energy Mater.* **10** 1903092
- [27] Ono L K, Raga S R, Wang S, Kato Y and Qi Y 2015 Temperature-dependent hysteresis effects in perovskite-based solar cells *J. Mater. Chem. A* **3** 9074–80
- [28] Mannino G, Alberti A, Deretzi I, Smecca E, Sanzaro S, Numata Y, Miyasaka T and La Magna A 2017 First evidence of $\text{CH}_3\text{NH}_3\text{PbI}_3$ optical constants improvement in a N_2 environment in the range 40–80 °C *J. Phys. Chem. C* **121** 7703–10
- [29] Dunbar R B, Moustafa W, Pascoe A R, Jones T W, Anderson K F, Cheng Y-B, Fell C J and Wilson G J 2017 Device pre-conditioning and steady-state temperature dependence of $\text{CH}_3\text{NH}_3\text{PbI}_3$ perovskite solar cells *Prog. Photovolt.* **25** 533–44
- [30] Cao R et al 2016 Unveiling the low-temperature pseudodegradation of photovoltaic performance in planar perovskite solar cell by optoelectronic observation *Adv. Energy Mater.* **6** 1600814
- [31] Zhang H, Qiao X, Shen Y, Moehl T, Zakeeruddin S M, Grätzel M and Wang M 2015 Photovoltaic behaviour of lead methylammonium triiodide perovskite solar cells down to 80 K *J. Mater. Chem. A* **3** 11762–7
- [32] Schwenzer J A, Rakocevic L, Gehlhaar R, Abzieher T, Gharibzadeh S, Moghadamzadeh S, Quintilla A, Richards B S, Lemmer U and Paetzold U W 2018 Temperature variation-induced performance decline of perovskite solar cells *ACS Appl. Mater. Interfaces* **10** 16390–9
- [33] Mesquita I, Andrade L and Mendes A 2019 Temperature impact on perovskite solar cells under operation *ChemSusChem* **12** 2186–94
- [34] Khan U, Zhinong Y, Khan A A, Zulfiqar A and Khan Q U 2019 Organic–inorganic hybrid perovskites based on methylamine lead halide solar cell *Sol. Energy* **189** 421–5
- [35] Khan U, Iqbal T, Khan M and Wu R 2021 SnO_2/ZnO as double electron transport layer for halide perovskite solar cells *Sol. Energy* **223** 346–50
- [36] Khan U, Zhinong Y, Khan A A, Zulfiqar A and Ullah N 2019 High-performance CsPbI_2Br perovskite solar cells with zinc and manganese doping *Nanoscale Res. Lett.* **14** 116
- [37] Yang R et al 2019 To reveal grain boundary induced thermal instability of perovskite semiconductor thin films for photovoltaic devices *IEEE J. Photovolt.* **9** 207–13
- [38] Lee T D and Ebong A U 2017 A review of thin film solar cell technologies and challenges *Renew. Sustain. Energy Rev.* **70** 1286–97
- [39] Dupré O, Vaillon R and Green M A 2015 Physics of the temperature coefficients of solar cells *Sol. Energy Mater. Sol. Cells* **140** 92–100
- [40] King D L, Kratochvil J A and Boyson W E 1997 Temperature coefficients for PV modules and arrays: measurement methods, difficulties, and results *Conf. Rec. 26th IEEE Photovolt. Spec. Conf.—1997* pp 1183–6
- [41] O'Donnell K P and Chen X 1991 Temperature dependence of semiconductor band gaps *Appl. Phys. Lett.* **58** 2924–6
- [42] Ishii T, Otani K, Takashima T and Kawai S 2011 Estimation of the maximum power temperature coefficients of PV modules at different time scales *Sol. Energy Mater. Sol. Cells* **95** 386–9
- [43] Liu S H, Simburger E J, Matsumoto J, Garcia I I A, Ross J and Nocerino J 2005 Evaluation of thin-film solar cell temperature coefficients for space applications *Prog. Photovolt.* **13** 149–56
- [44] McCandless B E and Sites J R 2010 Cadmium Telluride Solar Cells *Handbook of Photovoltaic Science and Engineering* pp 600–41
- [45] Kalvová J, Halenka T, Bezpalcová K and Nemešová I 2003 Köppen climate types in observed and simulated climates *Stud. Geophys. Geod.* **47** 185–202
- [46] Bhandari S, Roy A, Ali M S, Mallick T K and Sundaram S 2021 Cotton soot derived carbon nanoparticles for NiO supported processing temperature tuned ambient perovskite solar cells *Sci. Rep.* **11** 23388
- [47] Sadhukhan P, Roy A, Bhandari S, Mallick T K, Das S and Sundaram S 2023 Achieving high open circuit voltage for hole transport layer free ambient perovskite solar cells utilizing electric double layer effect *Sol. Energy Mater. Sol. Cells* **251** 112148
- [48] Kyakuno H, Fukasawa M, Ichimura R, Matsuda K, Nakai Y, Miyata Y, Saito T and Maniwa Y 2016 Diameter-dependent hydrophobicity in carbon nanotubes *J. Chem. Phys.* **145** 64514
- [49] Bhandari S, Roy A, Mallick T K and Sundaram S 2022 Morphology modulated brookite TiO_2 and BaSnO_3 as alternative electron transport materials for enhanced performance of carbon perovskite solar cells *Chem. Eng. J.* **446** 137378
- [50] Liang P-W, Liao C-Y, Chueh C-C, Zuo F, Williams S T, Xin X-K, Lin J and Jen A K-Y 2014 Additive enhanced crystallization of solution-processed perovskite for highly efficient planar-heterojunction solar cells *Adv. Mater.* **26** 3748–54
- [51] Sansoni S, De Bastiani M, Aydin E, Ugur E, Isikgor F H, Al-Zahrani A, Lamberti F, Laquai F, Meneghetti M and De Wolf S 2020 Eco-friendly spray deposition of perovskite films on macroscale textured surfaces *Adv. Mater. Technol.* **5** 1901009
- [52] Knight A J, Borchert J, Oliver R D J, Patel J B, Radaelli P G, Snaith H J, Johnston M B and Herz L M 2021 Halide segregation in mixed-halide perovskites: influence of A-site cations *ACS Energy Lett.* **6** 799–808

- [53] Chatterji N, Antony A and Nair P R 2019 Temperature coefficient of silicon-based carrier selective solar cells *IEEE J. Photovolt.* **9** 583–90
- [54] Ran C, Xu J, Gao W, Huang C and Dou S 2018 Defects in metal triiodide perovskite materials towards high-performance solar cells: origin, impact, characterization, and engineering *Chem. Soc. Rev.* **47** 4581–610
- [55] Kim H-S, Seo J-Y and Park N-G 2016 Material and device stability in perovskite solar cells *ChemSusChem* **9** 2528–40
- [56] Bhandari S, Roy A, Ghosh A, Mallick T K and Sundaram S 2020 Perceiving the temperature coefficients of carbon-based perovskite solar cells *Sustain Energy Fuels* **4** 6283–98
- [57] Meng Q, Chen Y, Xiao Y Y, Sun J, Zhang X, Han C B, Gao H, Zhang Y and Yan H 2021 Effect of temperature on the performance of perovskite solar cells *J. Mater. Sci., Mater. Electron.* **32** 12784–92
- [58] Zhou Q *et al* 2020 Understanding temperature-dependent charge extraction and trapping in perovskite solar cells *Adv. Funct. Mater.* **30** 2000550
- [59] Wang M, Yim W-L, Liao P and Shen Y 2017 Temperature dependent characteristics of perovskite solar cells *ChemistrySelect* **2** 4469–77
- [60] Feng Y, Zhang Y, Duan C, Zhao M and Dai J 2022 Optical properties of CsFAMA-based perovskite film and its application in the inverted solar cells with poly(methyl methacrylate) passivation layer *Opt. Mater. Express* **12** 3262–72
- [61] Calado P, Telford A M, Bryant D, Li X, Nelson J, O'Regan B C and Barnes P R F 2016 Evidence for ion migration in hybrid perovskite solar cells with minimal hysteresis *Nat. Commun.* **7** 13831
- [62] Yi H, Wang D, Duan L, Haque F, Xu C, Zhang Y, Conibeer G and Uddin A 2019 Solution-processed WO₃ and water-free PEDOT:PSS composite for hole transport layer in conventional perovskite solar cell *Electrochim. Acta* **319** 349–58
- [63] Zhang X, Guan Y, Zhang Y, Yu W, Wu C, Han J, Zhang Y, Chen C, Zheng S and Xiao L 2022 Achieving small temperature coefficients in carbon-based perovskite solar cells by enhancing electron extraction *Adv. Opt. Mater.* **10** 2201598